Numerical Simulation of Lightning Strike Damage to Wind Turbine Blades and Validation against Conducted Current Test Data

A.A.M. Laudani[1*], O. Vryonis[1], P.L. Lewin[1], I.O. Golosnoy[1], J. Kremer[2], H. Klein[2], O.T. Thomsen[3]

[1] The Tony Davies High Voltage Laboratory, School of Electronics and Computer Science, University of Southampton, University Road, Southampton, SO17 1BJ, United Kingdom

[2] Nordex Energy GmbH, Langenhorner Chaussee 600, Hamburg, 22419, Germany

[3] Bristol Composites Institute, Department of Aerospace Engineering, University of Bristol, Queen's Building, University Walk, Bristol, BS8 1TR, United Kingdom

[*]a.a.m.laudani@soton.ac.uk

ABSTRACT

This paper presents a novel numerical approach to simulate lightning strike damage to equipotential bonding interfaces of wind turbine blades, and model validation based on high-current testing. Modern rotor blades are equipped with metal receptors to intercept the lightning leader and metal down conductors to conduct the lightning current, preventing the direct attachment to the CFRP spars. In such conditions, damage in the form of resin thermal degradation and sparks develop inside the blade at the equipotential bonding interfaces. Excellent correlation was found between the numerical predictions and test results in terms of current and temperature distributions. High temperatures were predicted at the sparking areas observed in the tests, which suggested that the damage is thermally activated. Thermogravimetric analysis data indicated that the epoxy pyrolysis process evolves in stages, and that sparking events are often initiated by release of gases and formation of small voids at temperatures lower than expected.

Keywords: B. Delamination, C. Finite element analysis (FEA), Lightning protection, Wind turbine blade equipotential bonding.

1. Introduction

Rotor blades of large, modern wind turbines can reach up to 110 m in length in order to satisfy the increasing demand for higher rated power outputs [1]. In such conditions, the need of reducing the rotor blade weight without affecting the structural integrity has become essential. For this reason, wind turbine manufacturers have implemented carbon fibre reinforced polymer (CFRP) materials into the rotor blade load carrying laminates, i.e., the spar caps (see Fig. 1) [2–4]. However, the use of CFRP materials makes rotor blades highly sensitive to lightning strikes [5–7]. Consequently, it is required to equip them with a lightning protection system (LPS) capable of preventing damage due to lightning direct attachment. LPSs consist of an air termination system and a transmission system. The former is

typically composed of metal receptors placed over the blade surface near the tip. They are aimed to intercept the lightning leaders, to avoid the direct attachment to CFRP structures and the consequent damage modes, such as fibre and matrix damage [8,9]. The receptors should be designed against the IEC standard requirements [10] in order to transfer most of the lightning energy to the transmission system and withstand several lightning strikes without experiencing any damage [6]. The latter consists of metallic down conductor (DC) cables located in the blade cavity or braids encapsulated within the blade shell (see Fig. 1). They are intended to conduct the lightning current from the attachment point to the earthing system [10,11].

The incorporation of CFRP materials introduces additional challenges for the protection of the blade against lightning strikes. For instance, equipotential connections need to be realised between the DC and the CFRP structure to prevent internal arcs due to a high potential difference between the two conductors, which would cause severe structural damage to the spar [12–14]. However, this configuration splits the lightning current between the DC and CFRP spar, and thermal damage is usually observed at the bonding areas. In fact, the physical connections between the DC and the CFRP spar through equipotential bonding (EB) layers are obtained by epoxy resin during the infusion process of the blade [14]. Because of the presence of resin-rich areas, high values of contact resistance and temperatures are often found at the joint interfaces. These in turn lead thermal degradation of some of the resin around the EB points, sparking events, and potential delamination within the composite [14–18].

In order to produce an LPS design that resists lightning strikes, it is crucial to investigate how the lightning current propagates within the blade. This is usually accomplished by high-cost testing, which can be in excess of €100,000 including material and manufacturing of testing samples [14]. In recent years, numerical tools such as the finite element method (FEM) are increasingly used [14,16,19,20] to reduce the lightning testing costs. Once validated, a model can be re-employed several times during the design stage (e.g., geometry modifications and/or variation of the lightning waveform parameters might be necessary) at little extra cost [10,11,14,21]. Therefore, the objective of this study is to employ FEM simulations to predict the electromagnetic-thermal response of a CFRP rotor blade sample and the damage at the EB interfaces when subjected to simulated lightning current tests. In order to accomplish this, the epoxy resin infused in the test sample is subjected to thermogravimetric analysis (TGA) to determine the degradation reaction kinetics. The latter are then used in the FEM models to predict the polymer thermal degradation due to lightning strike induced temperature profiles.

Previous lightning studies used numerical simulations to predict the thermal damage due to lightning direct attachment to composite structures [22–24] or aircraft metal fasteners [25,26]. In contrast, this article considers the case when the lightning attaches at the receptor, and its current is conducted through the DC and CFRP spars. In such a scenario, damage in the form of resin thermal degradation and sparks develop at the EB interfaces because of current crowding and overheating, which has not been investigated before.

2. Technical Background

This study employs the FEM since one of the advantages of this method is the capability of computing spatial current density distributions in the cross-section of the blade LPS conductors.

This would allow to predict areas of high current density and the associated thermal damage at the EB interfaces [14]. On the other hand, previous research on simulation of lightning strikes to wind turbine blades was mainly based on equivalent circuit modelling [21,27], which are less computationally demanding but cannot provide spatial current density distributions in the blade cross-section [14]. In addition, this study includes key features of modern rotor blade geometries such as CFRP spars and equipotential connections, which introduce additional complications such as the current split between the DC and CFRP spar. Such components were instead disregarded in previous FEM studies [20] on lightning strikes to rotor blades.

The following set of input parameters and procedures are needed in the FEM model to predict the thermal damage at the EB interfaces:

- A procedure that solves for both electric scalar and magnetic vector potentials to capture the current split between the DC and spar, which was published in [14].
- The electrical and thermal conductivity values of CFRP materials, which were measured according to the experimental procedures presented in [28].
- The electrical contact resistivity values at the EB interfaces to predict accurate current density and temperature distributions, which were characterised and presented in [18].
- The thermal degradation reaction kinetics of the blade epoxy resin, which were determined by TGA experiments and presented in this paper.

3. Experimental

3.1. Materials

As a polymer matrix, a commercially available two-component epoxy system was employed (supplied by Hexion). It comprised of the Hexion RIMR035c epoxy resin and the amine-based Hexion RIMH037 curing agent. For the CFRP spar, a unidirectional (UD) non-crimp carbon fabric with an areal density of 870 g/m^2 (supplied by Saertex) was utilised. Biaxial (BIAX) non-crimp carbon fabric with 218 g/m^2 areal density (supplied by Saertex) was employed as EB between the copper LPS DC and the CFRP spar. Finally, the wind turbine blade sample was encapsulated within a BIAX non-crimp glass fabric with an areal density of 1,010 g/m^2 (supplied by Saertex).

3.2. Thermogravimetric Analysis

3.2.1. Sample Preparation

The epoxy resin samples were obtained by curing the Hexion epoxy system under vacuum. First, a flat mould was treated with 2-3 release agent layers to facilitate the de-moulding procedure. The Hexion RIMR035c epoxy resin was mixed with the Hexion RIMH037 hardener at a 100:20 ratio (as suggested by the manufacturer) and then degassed for 30 min in a vacuum chamber. A vacuum tube connected to a pump was placed in position to remove the air from the mould. After the completion of the degassing, the resin was poured into the mould while simultaneously applying vacuum. Finally, the resin was cured for 6 h at 70 °C [29–32], as suggested by the manufacturer.

3.2.2. Characterisation Procedure

The TGA experiment was performed using a Perkin Elmer Pyris 1 TGA analyser [33]. The assessed samples were subjected to the following heating procedure:

- Isothermal at 60 °C for 2 min in nitrogen environment.

- Heating from 60 °C to 900 °C at a constant heating rate in nitrogen environment.
- Isothermal at 900 °C for 30 min (in air environment, to burn residues and avoid blocking the device vents).
- End condition, i.e., cooling from 900 °C to 60 °C.

The above heating method was performed for the following heating rates: 0.2, 0.5, 1, 2, 5, 10, 20, 50, 100, 150, and 200 °C/min.

3.2.3. Polymer Thermal Degradation: Constituent Mechanisms and Theory

Thermogravimetry has been shown to be a useful tool for investigations of polymer thermal degradation. Although the pyrolysis process of cured epoxy resins is usually described as an apparent single reaction, in reality, it develops into multiple different mechanisms [34–36]. It has been established that epoxies display an initial degradation process, which involves release of water [37]. This initiation mechanism has been identified as a dehydration reaction between the hydroxyl (-OH) groups formed during crosslinking [32] and hydrogens originally found on the molecular backbone [37,38] (see Fig. 2). The latter process causes the formation of allylic ether groups (C-O-C groups adjacent to the unsaturated C=C), which are genuinely weaker and less stable than the original C-O groups, and allylic amine bonds in the case of amine-cured epoxies (C-N groups adjacent to the unsaturated C=C), which in turn are less stable than the original C-N bonds [34]. The latter results in a degradation mechanism which is occasionally mentioned as "head-to-head" degradation mechanism in the related literature [36] and is illustrated in Fig. 2. Eventually, another mechanism occurs via "random scission" processes of C-C bonds, a mechanism that might involve scission of aliphatic segments of higher molecular weight via the production of various combustible gases and hydrocarbons [34]. The two latter mechanisms exhibit similar activation energies and at sufficiently high heating rates they might overlap and even invert their sequence. Prior to any of the three described mechanisms, water molecules in the form of absorbed moisture might be released [35,39] (not to be confused with the described dehydration process). For convenience, the degradation reactions are, hereafter, abbreviated as follows: mechanism 1 (release of absorbed moisture), mechanism 2 (dehydration reaction), mechanism 3 (allylic bonds), mechanism 4 (random scission).

Although the heating rates achieved by laboratory TGA analysers are smaller than typical lightning ones, previous lightning protection studies [22,40], or similar high heating rate applications like laser processing of polymers [41,42], have modelled the pyrolysis process through the Arrhenius equation:

$$\frac{d\alpha}{dt} = \underbrace{\sum_{i=1}^{4} A_i[1-\alpha_i(t)]e^{-\frac{E_{a,i}}{RT_i}}}_{\text{Deconvoluted reactions description}} = \underbrace{A[1-\alpha(t)]^n e^{-\frac{E_a}{RT}}}_{\text{Apparent single reaction description}} \quad (1)$$

where $\frac{d\alpha}{dt}$ [1/s] is the degradation rate or reaction rate, t [s] is the time, A_i [1/s] is the pre-exponential factors of the i-th degradation mechanism, α_i(t) [1] is the degree of thermal degradation of the i-th degradation mechanism, $E_{a,i}$ [J/mol] is the activation energy of the i-th degradation mechanism, R [J/(mol·K)] is the molar gas constant, T_i [K] is the temperature of the i-th degradation mechanism, and n [1] is the reaction order.

The degree of thermal degradation of each mechanism is defined as [43]

$$\alpha_i(t) = \frac{m_p(t_0) - m_{p,i}(t)}{m_p(t_0) - m_{p,i}(t_\infty)}, \quad \alpha(t) = \sum_{i=1}^{4} \alpha_i(t) \tag{2}$$

where $m_p(t_0)$ [kg] is the initial polymer mass, $m_{p,i}(t)$ [kg] is the instantaneous polymer mass of the *i*-th degradation mechanism, and $m_{p,i}(t_\infty)$ [kg] is the final polymer mass of the *i*-th degradation mechanism.

3.2.4. Reaction Kinetics: Kissinger Method

The parameters E_a, n, and A define the pyrolysis process and are called reaction kinetics. In this study, they were computed through the Kissinger method [44,45]. It is a differential method based on the fact that, for a given heating rate, the first time derivative of the TGA curve (i.e., the DTGA curve) reaches a maximum at a certain temperature [45]:

$$\ln\left(\frac{\beta}{T_m^2}\right) = const - \frac{E_a}{R}\frac{1}{T_m} \tag{3}$$

where β [K/s] is the heating rate and T_m [K] is the temperature at maximum degradation rate.

The activation energy E_a is the energy required for the degradation reaction. It was determined from the slope of the linear plot presented in (3) after measuring experimental values of T_m at different β [44].

The reaction order expresses the degree of asymmetry of the DTGA curve [44]. It is equal to 1 when considering the deconvoluted description of the degradation process, assuming each degradation mechanism is randomly initiated. However, it is larger than 1 when considering the apparent single reaction description since the convoluted DTGA curve includes effected of different reactions. In this case, it was determined from the tangents at the inflection points of the DTGA curve [44]:

$$n = 1.26\sqrt{\left|\frac{\left(\frac{d^2\Gamma}{dt^2}\right)_{t=t_{Flex\,2}}}{\left(\frac{d^2\Gamma}{dt^2}\right)_{t=t_{Flex\,1}}}\right|} \tag{4}$$

where Γ[%] is the mass fraction of the polymer, $\frac{d^2\Gamma}{dt^2}$ [%/s^2] is the second time derivative of the mass fraction of the polymer, t_{Flex1} [s] is the time at the first inflection point, and t_{Flex2} [s] is the time at the second inflection point.

The inflection points were found where the second time derivative of the DTGA curve is zero [44]:

$$\frac{d^2}{dt^2}\left(\frac{d\Gamma}{dt}\right) = \frac{d^3\Gamma}{dt^3} = 0 \rightarrow (t_{Flex1}, t_{Flex2}) \tag{5}$$

where $\frac{d^3\Gamma}{dt^3}$ [%/s^3] is the third time derivative of the mass fraction of the polymer.

The first, second, and third time derivatives were computed from the TGA plots using OriginLab commercial software. To remove the experimental noise, the first time derivative plots of the low heating rate procedures were smoothed by the standard adjacent averaging method. The inflection points and the second time derivative values at the inflection points were found manually using the generated third and second time derivatives plots, respectively.

Finally, The pre-exponential factor defines the rate at which the pyrolysis reaction occurs and was found by [44]:

$$A = \frac{\frac{E_a\beta}{RT_m^2}}{\left[1 + (n-1)\frac{2RT_m}{E_a}\right]e^{-\frac{E_a}{RT_m}}} \tag{6}$$

3.3. Conducted Current Test

3.3.1. Wind Turbine Blade Tip Sample

The geometry of the assessed blade tip sample (arrangement and dimensions) is shown in Fig. 3 and represents an airfoil shell section of a 70 m wind turbine blade (see Fig. 1). It was composed of a 25 mm^2 copper braid (LPS DC) in parallel to a pultruded UD CFRP spar. The latter presented chamfered surfaces for mechanical purposes (note that the dimensions of each spar pultruded profile, i.e., the width, thickness, length, and chamfer angle, are not given for confidentiality reasons. However, the overall spar dimensions are provided). The two conductors were electrically bonded throughout the sample length (continuous-bonding configuration) by two layers of BIAX CFRP. To be consistent with the real blade structure, polyethylene (PET) foam was placed between the DC and the spar as a core material. In addition, the whole system (i.e., spar, DC, EB, and PET foam) was encapsulated within two layers of BIAX GFRP representing the blade shell (one placed on the top and one on the bottom of the sample). The sample was cured for 6 h at 75 °C following the vacuum assisted resin transfer moulding procedures, which is the standard manufacturing route for rotor blades [2–4]. Finally, the test sample impedance was not comparable to the full blade one since the specimen represented the blade tip only. Thus, copper bars were bolted to the sample root end to account for the impedance of the remaining blade section that was not manufactured.

3.3.2. Injected Current

The injected current is depicted in Fig. 4 and is the first positive short stroke [10], having time parameters t_1 = 19 μs and t_2 = 485 μs, and peak current I_0 = 125 kA.

3.3.3. Test Setup

The conducted current test was performed according to the standard procedures described in the IEC 61400-24:2019 [10]. The test setup is shown in Fig. 5, in which it is visible the sample under test, the generator, the return cage, and the measuring apparatus. The latter included four Rogowski coils and two oscilloscopes to measure the current at different sample locations, four cameras to collect sample pictures, and an infrared (IR) camera to record the sample temperature. The specimen was connected to the generator and return cage through copper bars. The current split between the DC and spar was measured at the Rogowski coil locations, indicated by red circles in Fig. 5.

3.3.4. Test Conditions

The test was conducted at a temperature of 16.6 °C and with a relative humidity of 50%.

4. Numerical

The test was simulated using COMSOL Multiphysics 5.5 in order to predict the damage due to the simulated lightning current.

4.1. Modelling Framework: Assumptions and Formulation

The following assumptions were made to model the electromagnetic-thermal response of wind turbine blades subjected to lightning strikes by the FEM:

- It was assumed that the air termination system can withstand several lightning strikes without experiencing any damage, in such a way that the majority of the lightning energy is conducted through the receptor and transferred to the DC. This is true if the air termination system is designed according to the procedures given in the IEC 61400-24:2019 standard [10].

- The rotor blade was considered reflectionless in this modelling approach, which has previously been shown to be a reasonable assumption [21].
- The displacement current density term was neglected in the electromagnetic formulation since lightning strikes are considered to be low-frequency applications [14].
- The heat transfer problem was solved by imposing a weak coupling with the electromagnetic problem, that is, no dependence of the electrical conductivity on temperature was considered. In fact, several studies such as [13,14,46] have shown that CFRP spar caps only conduct a small share of the lightning energy because of their low inductance and large resistance, and temperature lower than 100 °C are usually found in the bulk CFRP materials.

The electromagnetic field diffusion problem was computed by solving the following set of equations [47,48]:

$$\begin{cases} \nabla \text{ x } \boldsymbol{H} = \boldsymbol{J} \\ \nabla \cdot \boldsymbol{A} = 0 \\ \nabla \cdot \boldsymbol{J} = 0 \end{cases} \tag{7}$$

while the following relations are known:

$$\begin{cases} \boldsymbol{B} = \nabla \text{ x } \boldsymbol{A} \\ \boldsymbol{B} = \mu_0 \mu_r \boldsymbol{H} \\ \boldsymbol{J} = -\boldsymbol{\sigma} \nabla V - \boldsymbol{\sigma} \dfrac{d\boldsymbol{A}}{dt} \end{cases} \tag{8}$$

where ∇ x is the curl operator, $\boldsymbol{H}$ [A/m] is the magnetic field strength, $\boldsymbol{J}$ [A/m^2] is the current density, $\nabla \cdot$ is the divergence operator, $\boldsymbol{A}$ [Wb/m] is the magnetic vector potential, $\boldsymbol{B}$ [T] is the magnetic flux density, μ_0 [H/m] is the vacuum permeability, μ_r is the relative permeability, $\boldsymbol{\sigma}$ is the electrical conductivity tensor, ∇ is the gradient operator, V [V/m] is the electric scalar potential, and t [s] is the time.

The heat transfer problem was computed by solving for the heat diffusion equation [47,49]:

$$\rho \, C_p \frac{\partial T}{\partial t} + \nabla \cdot \boldsymbol{q_{cond}} = Q_{rh} \tag{9}$$

where ρ [kg/m^3] is the density, C_p [J/(kg·K)] is the specific heat capacity at constant pressure, T [K] is the temperature, $\boldsymbol{q_{cond}}$ [W/m^2] is the heat flux by conduction, and Q_{rh} [W/m^3] is the Joule heat.

The Joule heat due to the resistance of the individual blade components (i.e., DC, EB, and spar) and to the contact resistance at the EB interfaces was computed in the electromagnetic problem and applied to the heat transfer analysis through a weak coupling [48,49]:

$$Q_{rh} = \frac{1}{2}(\boldsymbol{J} \cdot \boldsymbol{E}) \tag{10}$$

where $\boldsymbol{E}$ [V/m] is the electric field strength.

Finally, the Arrhenius equation given in (1) was solved in the heat transfer problem via a weak coupling.

4.2. Material Properties

The properties of the blade materials and interfaces are listed in Table 1. The anisotropic electrical conductivities of both UD CFRP and BIAX CFRP were experimentally measured according to the procedures presented in [28]. The values of contact resistivity for BIAX EB joints are taken from [18]. The relative permittivity was assumed equal to 1 for both copper and CFRPs [40,50,51], whereas it was 4 for GFRP [52] and 1.7 for PET foam [53,54]. On the other hand, the relative permeability

Table 1. Properties of the blade materials.

Electrical, Magnetic, and Thermal Properties										
Materials	σ_{11} [S/m]	σ_{22} [S/m]	σ_{33} [S/m]	ε_r	μ_r	ρ [kg/m^3]	Cp [J/(kg·K)]	k_{11} [W/(m·K)]	k_{22} [W/(m·K)]	k_{33} [W/(m·K)]
UD CFRP (Spar)	40,365	132.900	51.700	1	1	1,335	1,200	2.500	0.900	0.710
BIAX CFRP (EB)	20,702	20,702	8.340	1	1	1,335	1,200	2.500	2.500	0.530
Copper (DC) [14,47]	5.998x10^7	5.998x10^7	5.998x10^7	1	1	8,960	385	400	400	400
PET foam (Core mat.) [62,63]	/	/	/	1.7	1	70	2,450	0.034	0.034	0.034
BIAX GFRP (Shell) [64–66]	/	/	/	4	1	1,600	850	0.740	0.740	0.340

Interface Contact Resistivity [18]	
Contact Area	ρ_C [mΩ·m^2]
C_DC-EB	0.031
C_EB-Spar	0.684
C_EB-Spar_Chamfer	7.583
C_PultrudedProfiles	6.413

was assumed equal to 1 for all the blade materials [55,56]. Finally, the CFRPs density, specific heat capacity at constant pressure, and longitudinal thermal conductivity were determined through the parallel rule of mixture [40,57–61]. In contrast, their transverse and through-thickness thermal conductivities were experimentally measured as specified in [28].

4.3. FEM Geometry and Mesh

The test sample geometry modelled in COMSOL Multiphysics 5.5 is shown in Fig. 6. To facilitate the meshing procedure, the EB layers 45° cuts at the tip and root ends were disregarded. The return cage used in the test needed to be implemented in the FEM model as a return path in order to obtain a comparable impedance and be consistent with the test. Thus, the blade sample was placed within an insulating computational domain having dimensions of 0.6 x 1.8 x 4.45 m. Each blade component was meshed using hexahedral elements, which is the suggested finite element type for electromagnetic-thermal problems [67–69]. In addition, boundary layers [47] were employed to reproduce the skin effect (crowding effect [70]) in the DC, as well as to capture the electric potential jump and the current distribution due to the contact resistance at the EB interfaces. After conducting a mesh convergence study (see Fig. 7), the FEM model was meshed by 97172 elements (see Fig. 6).

4.4. FEM Boundary Conditions

The current return path was defined by assuming magnetic and electric insulation conditions at the external boundaries of the insulating domain [48]:

$$\begin{cases} \mathbf{n} \times \boldsymbol{A} = 0 \\ \mathbf{n} \cdot \boldsymbol{J} = 0 \end{cases} \tag{11}$$

Electrical contact was modelled at the EB interfaces by assuming [48]

$$\begin{cases} \mathbf{n} \cdot \boldsymbol{J_1} = -\dfrac{1}{\rho_C}(V_1 - V_2) \\ \mathbf{n} \cdot \boldsymbol{J_2} = -\dfrac{1}{\rho_C}(V_2 - V_1) \end{cases} \tag{12}$$

A transient voltage boundary condition, shown in Fig. 8, was applied across the blade to inject the test current in the FEM

model. The procedure to compute the lightning transient voltage waveform is presented in [14].

Convective heat flux condition was assumed at the rotor blade external boundaries in contact with the ambient [47,49]:

$$-\boldsymbol{n} \cdot \boldsymbol{q_{conv}} = h(T_{ext} - T) \tag{13}$$

where $\boldsymbol{q_{conv}}$ [W/m^2] is the convective heat flux, h [W/(m^2·K)] is the heat transfer coefficient, and T_{ext} [K] is the ambient temperature. The air heat transfer coefficient was equal to 25 W/(m^2·K) [47,49].

Thermal radiation condition was assumed at the rotor blade external boundaries in contact with the ambient [47,49]:

$$-\boldsymbol{n} \cdot \boldsymbol{q_{rad}} = \varepsilon \sigma_{SB}(T_{ext}^4 - T^4) \tag{14}$$

where $\boldsymbol{q_{rad}}$ [W/m^2] is the radiative heat flux, ε is the emissivity, and σ_{SB} [W/(m^2·K^4)] is the Stefan-Boltzmann constant. The emissivity of CFRP and GFRP surfaces were equal to 0.9 [22] and 0.85 [71], respectively.

5. Results and Discussion

5.1. Epoxy Thermal Degradation: Apparent Single Reaction TGA and DTGA Curves

The TGA curves describing the epoxy thermal degradation process are shown in Fig. 9*a* for the assessed heating rates. Values of degradation onset temperature, T_{onset} [K], can be extrapolated from the TGA curves according to the procedures reported in the ASTM E2550-17 standard [72]. They are given by the intersection of the baseline (horizontal line) and the tangent line after the degradation occurs [72]. On the other hand, the first derivative of the TGA curves (see the DTGA curves plotted in Fig. 9*b*) allows to determine the temperature at maximum degradation rate. Both T_{onset} and T_m values increase with higher heating rates [60], as shown in Fig. 9.

5.2. Epoxy Thermal Degradation: Deconvoluted Reactions TGA and DTGA Curves

The experimental DTGA curves have been deconvoluted, by the Voigt model [73], into individual curves representing the different degradation mechanisms (see Fig. 10). The Voigt model has resulted in a better agreement between the convolution of the individual curves (red profiles) and the experimental DTGA curves (black profiles), compared with other models such as Gauss and Lorentz.

As expected, the results show that the degradation process starts with either mechanism 1 or 2, depending on the heating rate. It is revealed that mechanism 1 is only visible at heating rates above 5 °C/min, where its T_m appears to be ~100 °C. This mechanism does not constitute an epoxy degradation reaction *per se*, and its magnitude and/or presence might be situational and largely affected by environmental factors. In view of these factors, we do not consider discussing it further. Finally, Fig. 10 shows that the majority of the mass loss is caused by mechanisms 3 and 4. However, mechanism 2 cannot be ruled out as a potential degradation mechanism, although its contribution to the total degradation is between 2-3%. This is because even such a small amount of gas is sufficient to introduce voids that separate the rotor blade current carrying conductors and ignite sparks (see Section 5.6).

5.3. Degradation Reaction Kinetics

The degradation reaction kinetics, calculated by the Kissinger method [44,45] (see Section 3.2.4), are provided in Table 2 for

Table 2. Degradation reaction kinetics for both the apparent single reaction and the deconvoluted reactions models.

Reaction Kinetics	Apparent	Deconvoluted Reactions			
	Single Reaction	Mechanism 1	Mechanism 2	Mechanism 3	Mechanism 4
A [1/s]	2.20×10^{12}	13.11×10^{6}	2.00×10^{12}	4.76×10^{12}	2.19×10^{13}
n	1.17	1	1	1	1
E_a [kJ/mol]	185.78	64.86	137.36	188.06	200.22

both the apparent single reaction and the deconvoluted reactions models. These parameters can be used to model the degradation process by entering them into (1).

5.4. Lightning Current Distribution within the Wind Turbine Blade Conductors

The FEM simulation is capable of predicting the overall lightning current split between the blade conductors at different locations of the blade, as shown in Figs. 11*a* to 11*e*. The FEM currents are obtained by integrating the current density over the conductors' cross-section at the x-coordinates given in Fig. 5, indicating the locations of the Rogowski coils (the latter are represented by red circles in Fig. 5). The spar cross-sections at the specified x-coordinates can be derived from the overall spar width and thicknesses provided in Figs. 3 and 5, respectively. As shown in Figs. 11*a* to 11*e*, an excellent agreement is found between the test measurements and the FEM predictions, with negligible deviations in terms of peak current and specific energy due to geometrical approximations. As expected, the results show that during the rise front the lightning current is mainly conducted by the spar because of its low inductance, whereas during the slow decay front the lightning current mainly flows through the DC due to its low resistance. In addition, Fig. 11*f* illustrates how the peak current, measured by the Rogowski coils (see Fig. 5 for their locations), is redistributed along the DC and spar. It is observed that the continuous-bonding configuration allows the current to leave the spar and return to the DC gradually along the sample length. More specifically, the peak of the current flowing in the middle of the spar (Spar Current 1) is 75% of the injected current peak, while it reduces to 65% at the end of the fourth chamfer profile (Spar Current 2). This means that 10% of the current was diverted back to the DC. Furthermore, the peak of the current in the DC at the root is 47% of the total, which means that an additional 12% leaves the spar for the DC at the root end.

High current density areas (see Fig. 12) are predicted around the bonding interfaces at x = 3.4 m (position of the spar first pultruded profile). The high current density area at the EB-Spar interface is found where the current enters the spar first pultruded profile and is due to the large spar chamfer angle. The high current density area at the DC-EB interface is instead caused by the crowding effect in the DC, which reduces the contact area established with the EB layers required to divert the current to the spar [14]. These regions might lead to high temperatures and thermal damage due to Joule heating.

Finally, no significant difference in terms of overall current split is observed in Fig. 11 when simulating the test with electrical contact resistivities implemented at the bonding interfaces (blue curves) and without, i.e., ideal contact is assumed (red curves). This is expected as the resulting contact resistances are between 2 and 4 orders of magnitude smaller than the total impedance of the sample. On the other hand, the implementation

of the electrical contact affects the current density distribution in the EB joint cross-section. In fact, the high current density areas predicted at the bonding interfaces present different magnitudes when comparing the results of the two formulations given in Figs. 12*a* and 12*b*. More specifically, the maximum value of current density varies by a factor of 2.5 at the EB-Spar interface and by a factor of 2 at the DC-EB interface.

5.5. Temperature Distribution within the Wind Turbine Blade Conductors

Fig. 13 depicts the temperature distribution within the rotor blade sample at x = 3.4 m when modelling the electrical contact. As shown in Fig. 13*a*, the temperature within the spar does not exceed 90 °C. This is due to the fact that the spar conducts the lightning current for a short interval [13,14,46], as well as because the test sample presents EB layers over the spar chamfered surfaces. This allows the current to be injected through the entire spar cross-section, which reduces the Joule heating due to the CFRP anisotropy [18]. As the spar maximum temperature is considerably below the temperature dependence range of CFRP electrical and thermal conductivities [40,74], the weak coupling between the electromagnetic and heat transfer problems is a valid approach to model lightning strikes to wind turbine blades. On the other hand, large temperatures are achieved at the bonding interfaces because of high current density areas, as seen in Fig. 12. More specifically, a peak temperature of ~1,730 °C is achieved after ~33 μs at the EB-Spar interface (see Fig. 13*b*), whereas a peak value of 3,440 °C is observed after ~34 μs at the DC-EB interface (see Fig. 13*c*). After 38 s, the sample has cooled down and its temperature has approximately returned to ambient value.

The temperature distribution on the external surface of the sample (i.e., the GFRP shell inner layer) was recorded during the test through the IR camera. The results show that the temperature peak is attenuated and delayed through the shell compared with the temperature peak at the EB interfaces. For instance, a maximum value of ~32 °C is achieved after 1.7 s at the shell inner layer (see Fig. 14). Such a long delay is due to the low diffusivity of GFRP materials, which is equal to 2.5×10^{-7} m^2/s in the through-thickness direction. Hot areas at the shell inner layer are located between the DC and the spar and along the edge of the first pultruded profile where the lightning current enters the spar (see Fig. 14*a*). A good correlation is found with the FEM simulations regarding the temperature distribution in these regions of the sample (see Fig. 14*b*), although slight differences are noticed. For instance, the size of the hot area between the DC and spar (i.e., the red area in Figs. 14*a* and 14*b*) is slightly smaller in the simulation (see Fig. 14*b*) than in the test (see Fig. 14*a*). This may be due to the sparking events occurring in this area (see Section 5.6). The formation of voids and sparks may modify the contact area, which causes the current to spread over a larger area when it diverts towards the spar. The change in contact resistivity due to the sparks is not known and thus not implemented in the FEM model. In addition, the simulation predicts slightly higher temperatures in the region between the DC and spar (see Fig. 14*c*). In fact, both the peak temperature at 1.7 s and the temperature at 38 s are slightly overestimated by ~1 °C in the FEM simulation. This is caused by other two numerical assumptions. The first one is that the change in enthalpy of the system due to the epoxy degradation (see Section 5.6) is not modelled in the FEM simulation, which would dissipate part of the Joule heat. However, the increase in the solution accuracy

thanks to its implementation would not justify the significant growth of the computational time. The second one is represented by the employed contact resistivity values, which have been determined by room temperature low voltage tests while it is known that they decrease with increasing temperatures [18]. Despite the approximations and assumptions mentioned above, the overall FEM computations of heat release and temperature are accurate as the predicted hot regions correspond to the ones measured experimentally.

Finally, note that much lower temperatures are achieved at the EB interfaces if ideal contact is assumed, e.g., up to 465 °C at the EB-Spar interface (see Fig. 13*b*) and 930 °C at the DC-EB interface (see Fig. 13*c*). In addition, major temperature disagreements are also found, with ideal contact, at the shell inner layer, where the heating and cooling profiles are noticeably different compared with the test observations (see Fig. 14*c*). These discrepancies are expected as lower values of current density are achieved when considering the ideal contact formulation, as seen in Section 5.4. Therefore, it is essential to model the electrical contact at the EB interfaces in order to achieve accurate current density and temperature distributions.

5.6. Thermal Damage: Sparking and Delamination

Fig. 15*a* depicts the test sample during the conduction of the simulated lightning current, as well as the positions of the sample components (the dashed lines indicate that the component is encapsulated within the GFRP shell). As shown in the figure mentioned above, sparks have been observed at the tip end of the sample. They have developed along the DC edge on the spar side (no. 1) and along the edge of the first pultruded profile where the lightning current enters the spar (no. 2). In addition, a delamination of ca. 26.1x8.5 mm^2 has been observed in area no.1 (see Fig. 15*b*). It occurs between the BIAX EB layer and the inner surface of the GFRP shell outer layer in the vicinity of the DC (see Fig. 15*c*), which is visible thanks to the transparency of GFRPs. This delamination is most likely caused by the excessive heating at this location (see Fig. 13*c*) and the associated thermal stresses due to the thermal expansion mismatch between copper and composite materials [75,76].

The sparks and delamination observed in the test are located above the DC-EB and EB-Spar interfaces in the area around x = 3.4 m. That is, where high current densities (see Fig. 12*a*) and temperatures (see Figs. 13*b* and 13*c*) are found within the sample cross-section. By solving the Arrhenius equation in the FEM model using the thermal degradation kinetics and the temperature predicted at each time step, the degree of thermal degradation is computed. The results indicate the occurrence of polymer degradation at both DC-EB (see Fig. 15*d*) and EB-Spar (see Fig. 15*e*) interfaces in the area around 3.4 m, i.e., where sparks have been observed. More specifically, Fig. 15*d* shows that sparking area no. 1 coincides with the red area (i.e., $0.9 \leq \alpha \leq 1$) of both mechanisms 3 and 4. On the other hand, polymer degradation is predicted in proximity of sparking area no. 2 for mechanism 2 only (see Fig. 15*e*), as the temperature in this area is below the onset temperatures of mechanisms 3 and 4 (note that the temperature in area no. 2 is 800-1,000 °C, while the 1,730 °C peak is achieved on the EB vertical layer only, see Fig. 13*b*). In other words, the degradation in sparking area no. 2 would not be predicted if the apparent single reaction approach (i.e., all mechanisms summed together) was used, which would contradict the test observations. Considering these results, it is therefore concluded that sparking phenomena triggered at the EB

interfaces of wind turbine blades during lightning strikes are thermally activated. That is, epoxy degradation caused by high temperatures results in formation of gas filled voids, which separate the current carrying conductors and ignite sparks [15].

6. Conclusion

This article presents the development and predictions of an FEM model framework capable of simulating the electromagnetic-thermal behaviour and damage of a CFRP based rotor blade sample subjected to lightning high-current tests. Lightning damage to modern wind turbine blades typically develops at the LPS EB interfaces. Such regions present resin-rich areas that lead to high-current densities and temperatures, with consequent resin thermal degradation and sparking events.

It was shown that:

- numerical simulations are effective tools to study the thermal damage at the considered EB interfaces. In fact, the proposed FEM model predicted high current densities and temperatures at the sparking locations, which allowed a qualitative estimation of potential thermal degradation areas upon solution of the Arrhenius equation.
- The predictions of high temperature and thermal degradation at the sparking locations indicated that the damage is thermally activated. That is, high temperatures cause epoxy pyrolysis, leading to voids formation, separation of the blade current carrying conductors, and ignition of sparks.
- Even 2-3% of mass converted into a gas fraction is sufficient to displace the conductors carrying the current and ignite sparks, as in the case of mechanism 2. In fact, the latter was the only degradation mechanism predicted at sparking area no. 2, which would not be captured if the apparent single reaction description was used.
- The FEM formulations with and without the contact resistivities at the bonding interfaces presented major differences in terms of local current density and temperature distributions, e.g., peak temperatures were up to 4 times smaller in the ideal contact formulation. Therefore, it is essential to implement the electrical contact in the FEM models to compute accurate current density and temperature distributions and design reliable EB solutions.

7. Acknowledgment

This study was funded by Nordex Energy GmbH and the University of Southampton, grant agreement 0179210, and by the EU Horizon 2020 Marie Sklodowska-Curie Actions - Innovative Training Networks (ITN), grant agreements 642771 (SPARCARB project) and 734629 (PATH project).

8. References

[1] Merker K. HALIADE-X Shaping the Future. Presented at the Wind Mission Lithuania 2020 International Conference, unpublished, 2020.

[2] Thomsen OT. Sandwich materials for wind turbine blades - Present and future. J Sandw Struct Mater 2009;11:7–26. https://doi.org/10.1177/1099636208099710.

[3] Brøndsted P, Nijssen RPL. Advances in Wind Turbine Blade Design and Materials. Cambridge: Woodhead Publishing Limited; 2013. https://doi.org/10.1533/9780857097286.3.413.

[4] Mishnaevsky L, Branner K, Petersen HN, Beauson J, McGugan M, Sørensen BF. Materials for wind turbine blades: An overview. Materials (Basel) 2017;10:1–24. https://doi.org/10.3390/ma10111285.

[5] Rachidi F, Rubinstein M, Montanyà J, Bermúdez J, Sola RR, Solà G, et al. A Review of Current Issues in Lightning Protection of New-

Generation Wind-Turbine Blades. IEEE Trans Ind Electron 2008;55:2489–96. https://doi.org/10.1109/TIE.2007.896443.

[6] Montanyà J. Lightning interaction and damages to wind turbines. V Russ. Conf. Light. Prot., 2016, p. 1–15.

[7] Candela Garolera A, Madsen SF, Nissim M, Myers J, Holboell J. Lightning Damage to Wind Turbine Blades From Wind Farms in U.S. IEEE Trans Power Deliv 2016;31:1–1. https://doi.org/10.1109/TPWRD.2014.2370682.

[8] Chippendale RD, Golosnoy IO, Lewin PL. Numerical modelling of thermal decomposition processes and associated damage in carbon fibre composites. J Phys D Appl Phys 2014;47:1–15. https://doi.org/10.1088/0022-3727/47/38/385301.

[9] Harrell TM, Thomsen OT, Dulieu-Barton JM, Madsen SF. Damage in CFRP composites subjected to simulated lighting strikes - Assessment of thermal and mechanical responses. Compos Part B Eng 2019;176:107298. https://doi.org/10.1016/j.compositesb.2019.107298.

[10] International Electrotechnical Commission. IEC 61400 Ed. 2.0, Wind energy generation systems - Part 24: Lightning protection. Geneva: 2019.

[11] International Electrotechnical Commission. IEC62305, Protection against lightning Part 1: General principles. Geneva: 2010.

[12] Haigh S. Recommended Practices for Wind Turbine Testing - Lightning Protection for Wind Turbine Installations. 1997.

[13] Smorgonskiy A, Rachidi F, Rubinstein M. Modeling lightning current distribution in conductive elements of a wind turbine blade. Int. Conf. Light. Prot., IEEE; 2014, p. 1415–7. https://doi.org/10.1109/ICLP.2014.6973352.

[14] Laudani AAM, Carloni L, Thomsen OT, Lewin PL, Golosnoy IO. Efficient Method for the Computation of Lightning Current Distributions in Wind Turbine Blades using the Fourier Transform and the Finite Element Method. IET Sci Meas Technol 2020;14:786–99. https://doi.org/10.1049/iet-smt.2019.0343.

[15] Slade PG, editor. Electrical Contacts: Principles and Applications. 2nd Ed. Boca Raton, USA: CRC Press; 2017.

[16] Laudani AAM, Golosnoy IO, Thomsen OT, Lewin PL. Novel numerical models for the simulation of the electromagnetic response of CFRP wind turbine spars subjected to lightning strikes. Int. Conf. Light. Static Electr., Wichita, USA: 2019, p. 1–9.

[17] Rey Fernández JA, Montanya Puig J. Simulation of current distribution in a wind turbine blade using the FDTD method. Electr Power Syst Res 2020;185:1–7. https://doi.org/10.1016/j.epsr.2020.106350.

[18] Laudani AAM, Senis EC, Lewin PL, Golosnoy IO, Kremer J, Klein H, et al. Estimation of Contact Resistivity in Lightning Protection Equipotential Bonding Joints of Wind Turbine Blades. IEEE Trans Electromagn Compat 2021;63:1163–78. https://doi.org/10.1109/TEMC.2021.3059365.

[19] Laudani AAM, Golosnoy IO, Thomsen OT. Numerical computation of lightning time-domain voltages using the Fourier analysis and the finite element method. Tenth Int. Conf. Comput. Electromagn., Edinburgh, GB: 2019, p. 1–6. https://doi.org/10.1049/cp.2019.0110.

[20] Mucsi V, Ayub AS, Muhammad-Sukki F, Zulkipli M, Muhtazaruddin MN, Saudi ASM, et al. Lightning protection methods for wind turbine blades: An alternative approach. Appl Sci 2020;10:1–18. https://doi.org/10.3390/app10062130.

[21] Candela Garolera A, Holboell J, Madsen SF. Lightning transient analysis in wind turbine blades. Proc. Int. Conf. Power Syst. Transients, Vancouver, Canada: 2013, p. 8.

[22] Ogasawara T, Hirano Y, Yoshimura A. Coupled thermal-electrical analysis for carbon fiber/epoxy composites exposed to simulated lightning current. Compos Part A Appl Sci Manuf 2010;41:973–81. https://doi.org/10.1016/j.compositesa.2010.04.001.

[23] Wang Y, Zhupanska OI. Lightning strike thermal damage model for glass fiber reinforced polymer matrix composites and its application to wind turbine blades. Compos Struct 2015;132:1182–91. https://doi.org/10.1016/j.compstruct.2015.07.027.

[24] Zhao Y, Yang B, Zhang Y. Experimental Research and Simulation Analysis of Lightning Ablation Damage Characteristics of Megawatt Wind Turbine Blades. Metals (Basel) 2021;11. https://doi.org/https://doi.org/10.3390/met11081251.

[25] Chemartin L, Lalande P, Peyrou B, Chazottes A, Elias PQ, Delalondre C, et al. Direct Effects of Lightning on Aircraft Structure : Analysis of the Thermal , Electrical and Mechanical Constraints. J Aerosp Lab 2012;9:1–15.

[26] Chemartin L, Lalande. P, Tristant F. Modeling and Simulation of Sparking in Fastenning Assemblies. Int. Conf. Light. Static Electr., Seattle, USA: 2013, p. 1–7.

[27] Candela Garolera A. Lightning protection of flap system for wind turbine blades. Technical University of Denmark, PhD Thesis, 2014. https://doi.org/http://dx.doi.org/10.1016/j.epsr.2012.07.017.

[28] Senis EC, Golosnoy IO, Dulieu-Barton JM, Thomsen OT. Enhancement of the electrical and thermal properties of unidirectional carbon fibre/epoxy laminates through the addition of graphene oxide. J Mater Sci 2019;54:8955–70. https://doi.org/10.1007/s10853-019-03522-8.

[29] Vryonis O, Andritsch T, Vaughan AS, Lewin PL. An alternative synthesis route to graphene oxide: influence of surface chemistry on charge transport in epoxy-based composites. J Mater Sci 2019;54:8302–18. https://doi.org/10.1007/s10853-019-03477-w.

[30] Vryonis O, Andritsch T, Vaughan AS, Lewin PL. Structural and chemical comparison between moderately oxygenated and edge oxygenated graphene: mechanical, electrical and thermal performance of the epoxy nanocomposites. SN Appl Sci 2019;1:1–10. https://doi.org/10.1007/s42452-019-1303-9.

[31] Vryonis O, Andritsch T, Vaughan AS, Lewin PL. Effect of surfactant molecular structure on the electrical and thermal performance of epoxy/functionalized-graphene nanocomposites. Polym Compos 2020:1–15. https://doi.org/10.1002/pc.25573.

[32] Vryonis O, Virtanen STH, Andritsch T, Vaughan AS, Lewin PL. Understanding the cross-linking reactions in highly oxidized graphene/epoxy nanocomposite systems. J Mater Sci 2019;54:3035–51. https://doi.org/10.1007/s10853-018-3076-8.

[33] Perkin Elmer Incorporated. Pyris 1 TGA Thermogravimetric Analyzer. 2013.

[34] Levchik S V., Weil ED. Thermal decomposition, combustion and flame-retardancy of epoxy resins - A review of the recent literature. Polym Int 2004;53:1901–29. https://doi.org/10.1002/pi.1473.

[35] Kathmann SM, Palmer BJ, Schenter GK, Garrett BC. Activation energies and potentials of mean force for water cluster evaporation. J Chem Phys 2008;128. https://doi.org/10.1063/1.2837282.

[36] Menczel JD, Bruce Prime R, editors. Thermal Analysis of Polymers - Fundamentals and Applications. Hoboken, USA: Wiley; 2009.

[37] Bishop DP, Smith DA. The Thermal Degradation of Expoxide Resins. Ind Eng Chem 1967;59:32–9.

[38] Rose N, Le Bras M, Bourbigot S, Delobel R. Thermal oxidative degradation of epoxy resins: evaluation of their heat resistance using invariant kinetic parameters. Polym Degrad Stab 1994;45:387–97. https://doi.org/10.1016/0141-3910(94)90209-7.

[39] Grassie N, Guy MI, Tennent NH. Degradation of epoxy polymers: 2-Mechanism of thermal degradation of bisphenol-A diglycidyl ether. Polym Degrad Stab 1985;13:11–20. https://doi.org/10.1016/0141-3910(85)90131-4.

[40] Wang Y. Multiphysics analysis of lightning strike damage in laminated carbon/glass fiber reinforced polymer matrix composite materials: A review of problem formulation and computational modeling. Compos Part A Appl Sci Manuf 2017;101:543–53. https://doi.org/10.1016/j.compositesa.2017.07.010.

[41] Bityurin N, Luk'yanchuk BS, Hong MH, Chong TC. Models for laser ablation of polymers. Chem Rev 2003;103:519–52. https://doi.org/10.1021/cr010426b.

[42] Ou Y, Wu J, Zhang Y, Li J. Modeling the laser-polymer interaction of laser propulsion systems considering progressive surface removal, thermal decomposition and non-Fourier effect. Acta Astronaut 2021;186:319–28. https://doi.org/10.1016/j.actaastro.2021.05.042.

[43] Hu Y, Wang Z, Cheng X, Ma C. Non-isothermal TGA study on the combustion reaction kinetics and mechanism of low-rank coal char. RSC Adv 2018;8:22909–16. https://doi.org/10.1039/C8RA02618A.

[44] Kissinger HE. Reaction Kinetics in Differential Thermal Analysis. Anal Chem 1957;29:1702–6. https://doi.org/10.1021/ac60131a045.

[45] Chairat A, Joulia X, Floquet P, Vergnes H, Ablitzer C, Fiquet O, et al. Thermal degradation kinetics of a commercial epoxy resin - Comparative analysis of parameter estimation methods. J Appl Polym Sci 2015;132:6–9. https://doi.org/10.1002/app.42201.

[46] Nunes de Souza LF, Librantz H, Amonrim J, Adabo G. Analysis of Direct Effects of Lightning on Composite. IX Int. Symp. Light. Prot., Foz Do Iguaçu, Brazil: 2007.

[47] Comsol 5.6. Comsol Multiphysics Reference Manual. 2020.

[48] Comsol 5.6. AC / DC Module User 's Guide. 2020.

[49] Comsol 5.6. Heat Transfer Module. 2020.

[50] Todoroki A. Skin effect of alternating electric current on laminated CFRP. Adv Compos Mater 2012;21:477–89. https://doi.org/10.1080/09243046.2012.743716.

[51] Abid R. Electrical Characterisation of Aerospace Grade Carbon-Fibre-

Reinforced Polymers. Cardiff University, PhD Thesis, 2015.

[52] Madsen SF. Interaction between electrical discharges and materials for wind turbine blades – particularly related to lightning protection. Technical University of Denmark, PhD Thesis, 2006.

[53] Yan J, Wang G, Ma Y, Guo Z, Ren H, Zhang L, et al. Electrical and thermal performance of different core materials applied in wind turbine blades under lightning strikes. Wind Energy 2019;22:1603–21. https://doi.org/10.1002/we.2392.

[54] Yan J, Wang G, Li Q, Zhang L, Yan JD, Chen C, et al. A comparative study on damage mechanism of sandwich structures with different core materials under lightning strikes. Energies 2017;10. https://doi.org/10.3390/en10101594.

[55] Galehdar A, Nicholson KJ, Callus PJ, Rowe WST, John S, Wang CH, et al. The strong diamagnetic behaviour of unidirectional carbon fiber reinforced polymer laminates. J Appl Phys 2012;112:2–8. https://doi.org/10.1063/1.4764041.

[56] Tzeng JT, Hsieh KT. Electromagnetic field effect and analysis of composite structure. IEEE Trans Plasma Sci 2015;43:1536–40. https://doi.org/10.1109/TPS.2015.2404136.

[57] Mouritz AP, Feih S, Kandare E, Mathys Z, Gibson AG, Des Jardin PE, et al. Review of fire structural modelling of polymer composites. Compos Part A Appl Sci Manuf 2009;40:1800–14. https://doi.org/10.1016/j.compositesa.2009.09.001.

[58] Koráb J, Štefánik P, Kavecký Š, Šebo P, Korb G. Thermal conductivity of unidirectional copper matrix carbon fibre composites. Compos - Part A Appl Sci Manuf 2002;33:577–81. https://doi.org/10.1016/S1359-835X(02)00003-9.

[59] Sweeting RD, Liu XL. Measurement of thermal conductivity for fibre-reinforced composites. Compos Part A Appl Sci Manuf 2004;35:933–8.

[60] Mouritz AP, Gibson A. Fire Properties of Polymer Composite Materials. Dordrecht, The Netherlands: Springer; 2006. https://doi.org/10.1007/978-1-4020-5356-6.

[61] Newcomb BA. Processing, structure, and properties of carbon fibers. Compos Part A Appl Sci Manuf 2016;91:262–82. https://doi.org/10.1016/j.compositesa.2016.10.018.

[62] Almanza O, Rodríguez-Pérez MA, de Saja JA. Measurement of the thermal diffusivity and specific heat capacity of polyethylene foams using the transient plane source technique. Polym Int 2004;53:2038–44. https://doi.org/10.1002/pi.1624.

[63] Armacell. ArmaForm ® Core GR. 2020.

[64] Kasen MB. Mechanical and thermal properties of filamentary-reinforced structural composites at cryogenic temperatures 1: Glass-reinforced composites. Cryogenics (Guildf) 1975;15:327–49. https://doi.org/10.1016/0011-2275(75)90079-X.

[65] Kalogiannakis G, Van Hemelrijck D, Van Assche G. Measurements of thermal properties of carbon/epoxy and glass/epoxy using modulated temperature differential scanning calorimetry. J Compos Mater 2004;38:163–75. https://doi.org/10.1177/0021998304038647.

[66] Suchitra M, Renukappa NM. The Thermal Properties of Glass Fiber Reinforced Epoxy Composites with and without Fillers. Macromol Symp 2016;361:117–22. https://doi.org/10.1002/masy.201400227.

[67] Zhou P. Numerical Analysis of Electromagnetic Fields. Berlin, Germany: Springer-Verlag; 1993.

[68] Gasmi N, Bouissou S, Piriou F. Comparison of Potential Dual Formulations Developed with Different Elements. In: Nicolet A, Belmans R, editors., Boston, USA: Springer; 1995.

[69] Meunier G, editor. The Finite Element Method for Electromagnetic Modeling. Hoboken, USA: Wiley; 2008.

[70] Dwight HB. Skin effect in tubular and flat conductors. Trans Am Inst Electr Eng 1918;37:1379–403. https://doi.org/10.1109/T-AIEE.1918.4765575.

[71] Wang Y. Modeling of lightning-induced thermal ablation damage in anisotropic composite materials and its application to wind turbine blades. University of Iowa, PhD Thesis, 2016.

[72] ASTM International. ASTM E2550-17 Standard Test Method for Thermal Stability by Thermogravimetry. 2017.

[73] Perejón A, Sánchez-Jiménez PE, Criado JM, Pérez-Maqueda LA. Kinetic analysis of complex solid-state reactions. A new deconvolution procedure. J Phys Chem B 2011;115:1780–91. https://doi.org/10.1021/jp110895z.

[74] Abdelal G, Murphy A. Nonlinear numerical modelling of lightning strike effect on composite panels with temperature dependent material properties. Compos Struct 2014;109:268–78. https://doi.org/10.1016/j.compstruct.2013.11.007.

[75] Ishikawa T, Nagao T, Kobayashi A, Shimizu M, Hattori A, Kawano H.

Reduction of thermal stress induced in a steel plate strengthened by bonded aluminum-CFRP composite. Adv Struct Eng 2014;17:1771–83. https://doi.org/10.1260/1369-4332.17.12.1771.

[76] Wu T, Tinkloh SR, Tröster T, Zinn W, Niendorf T. Determination and Validation of Residual Stresses in CFRP/Metal Hybrid Components Using the Incremental Hole Drilling Method. J Compos Sci 2020;4:143. https://doi.org/10.3390/jcs4030143.

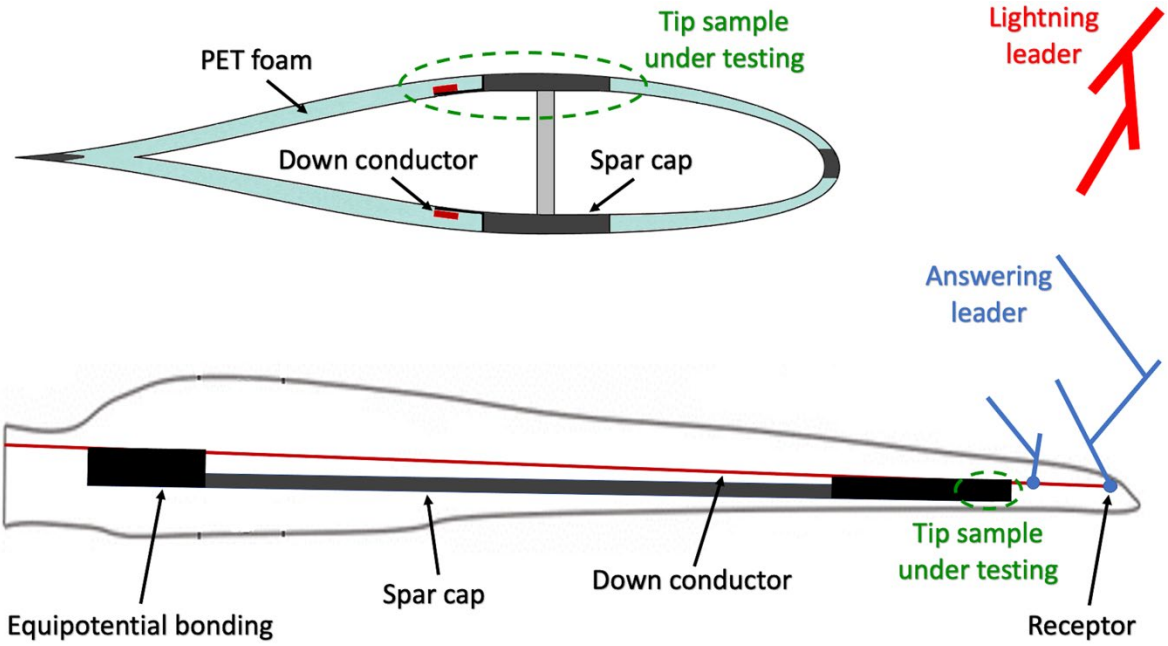

Fig. 1. Wind turbine blade schematic and location of the tip sample under testing.

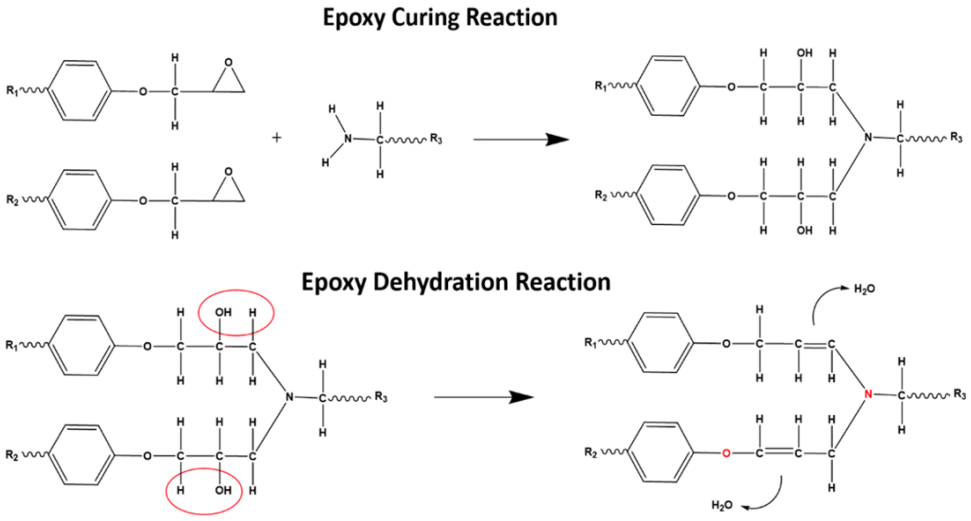

Fig. 2. Epoxy curing reaction (via reaction with amine hardener) with formation of hydroxyl (-OH) groups and epoxy dehydration reaction via water formation and subsequent removal and formation of allylic ether (C-O-C) and nitrogen (C-N) bonds (coloured red).

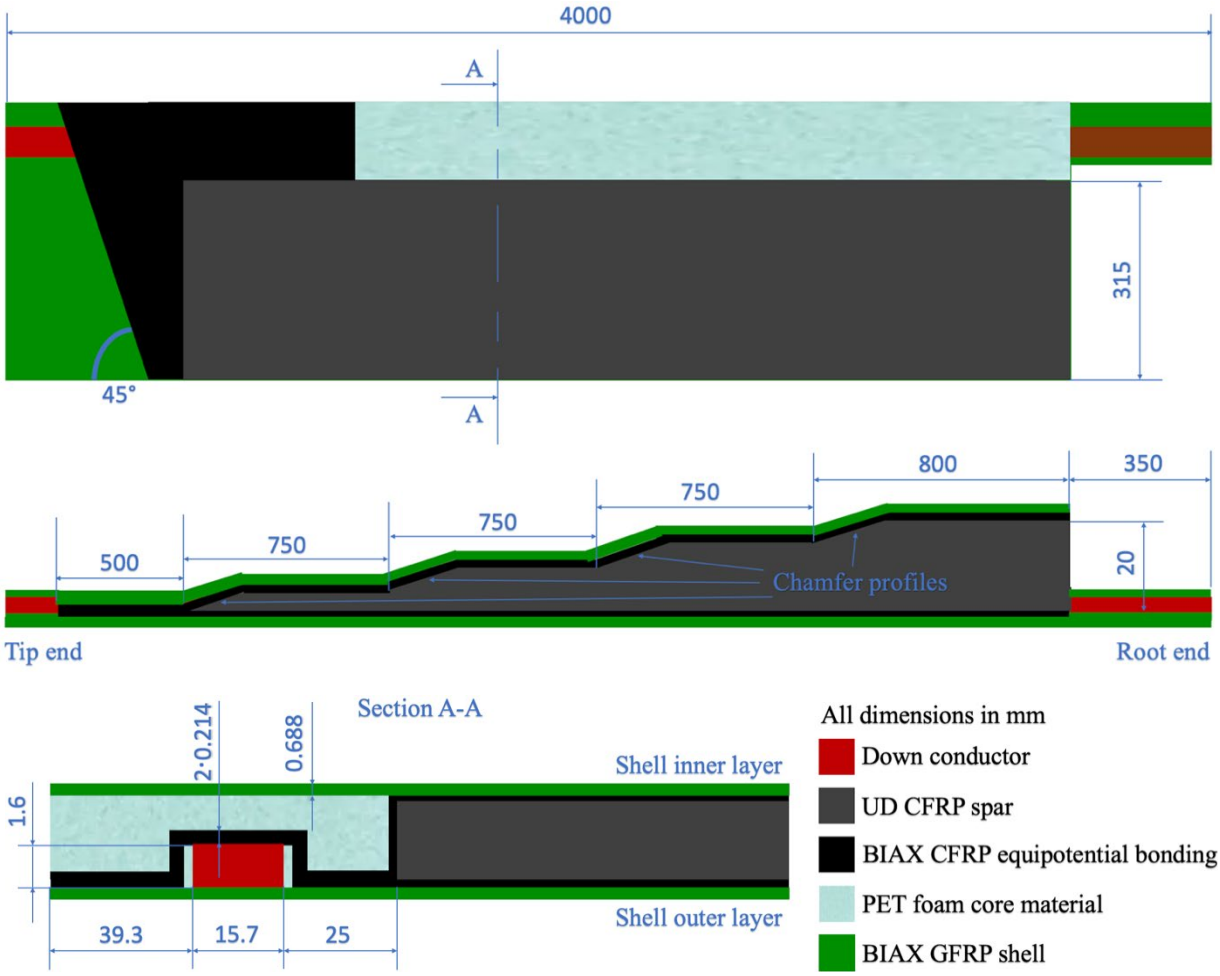

Fig. 3. Wind turbine blade sample under testing (not to scale). In the top view, both the shell inner layer and the top EB layer were intentionally omitted to show the DC and the spar.

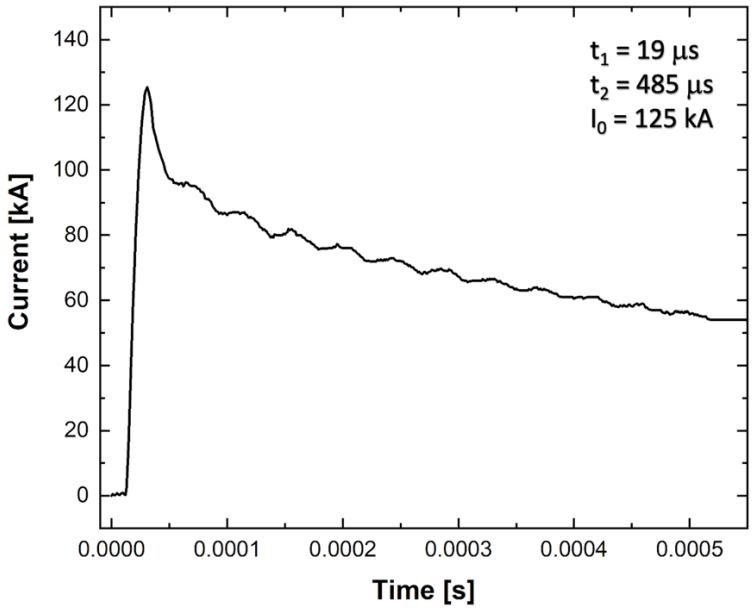

Fig. 4. Conducted current test: injected current.

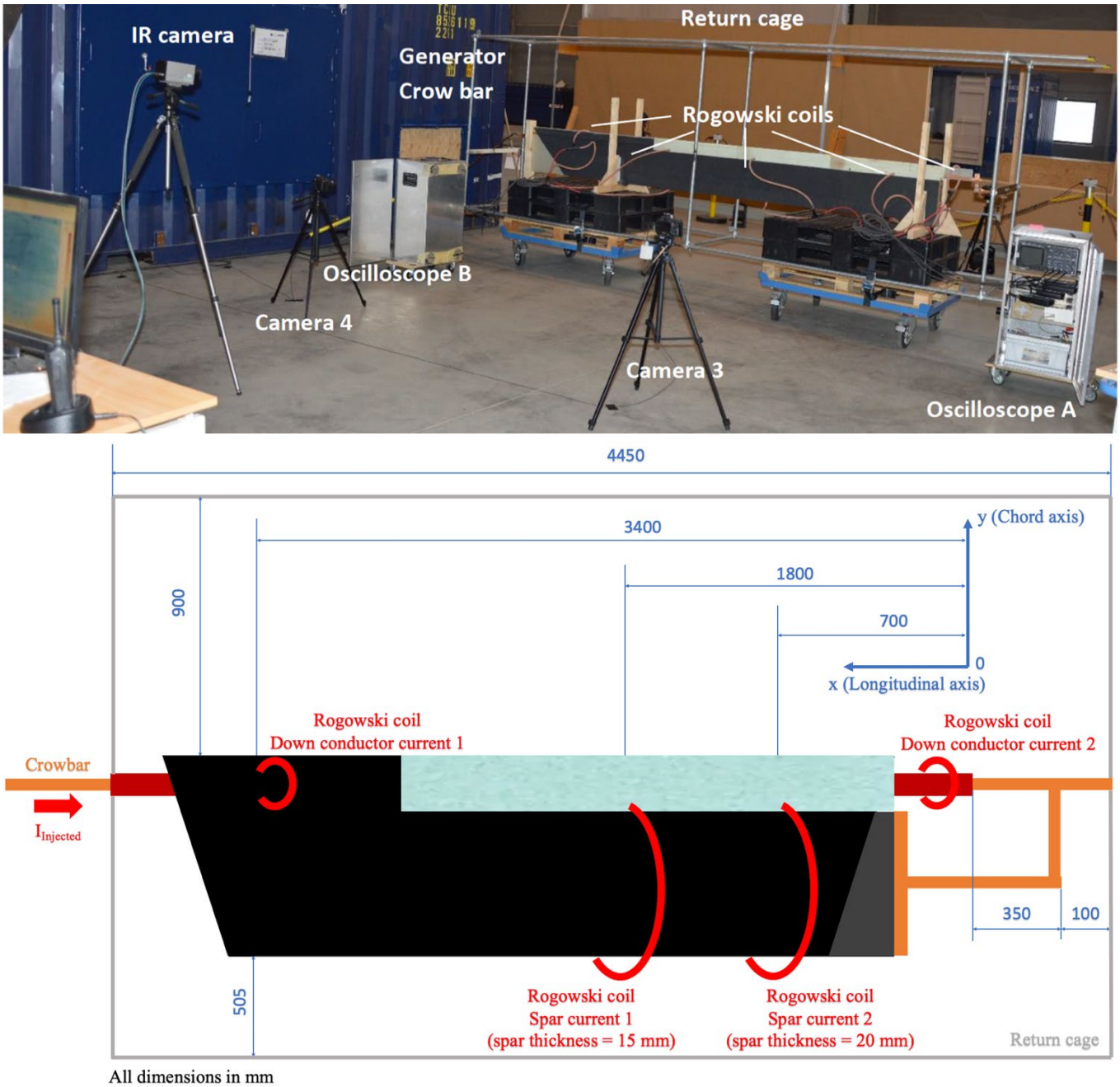

Fig. 5. Test setup of the conducted current test. Both the inner and outer layers of the shell were intentionally omitted to show the sample conductors.

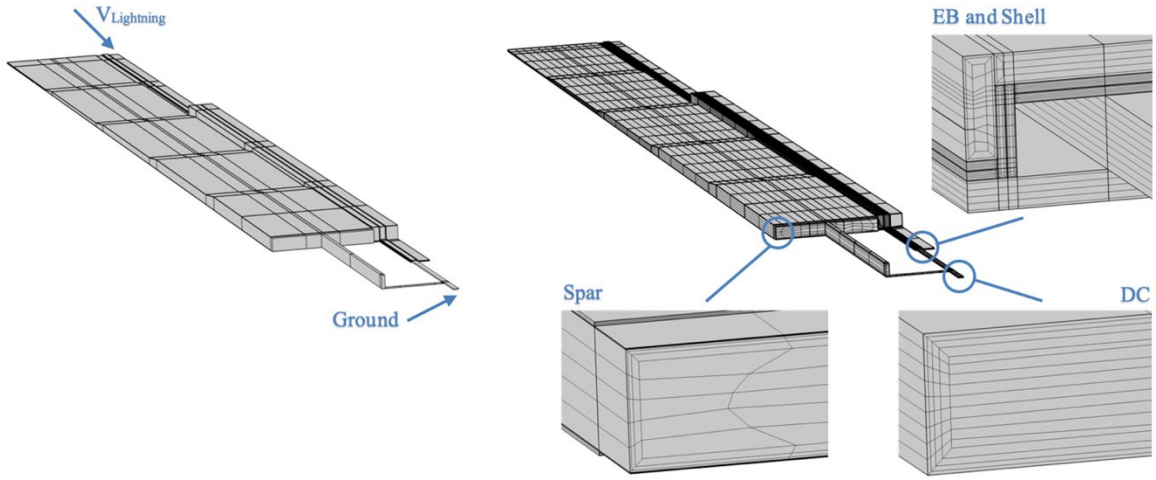

Fig. 6. FEM geometry and mesh (the insulating domain is intentionally hidden).

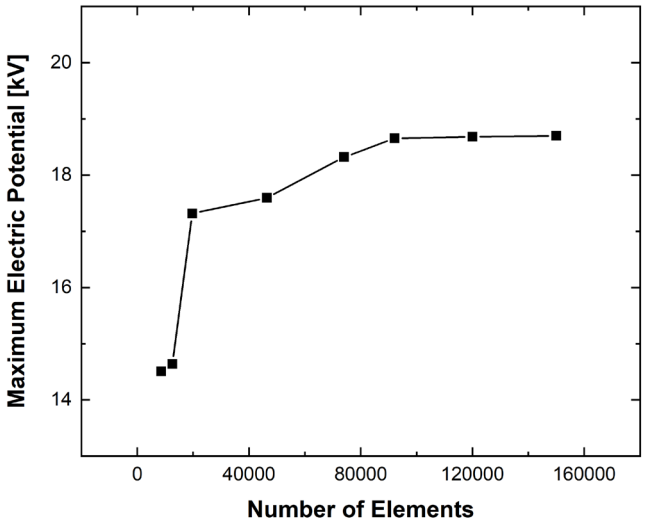

Fig. 7. Mesh convergence study.

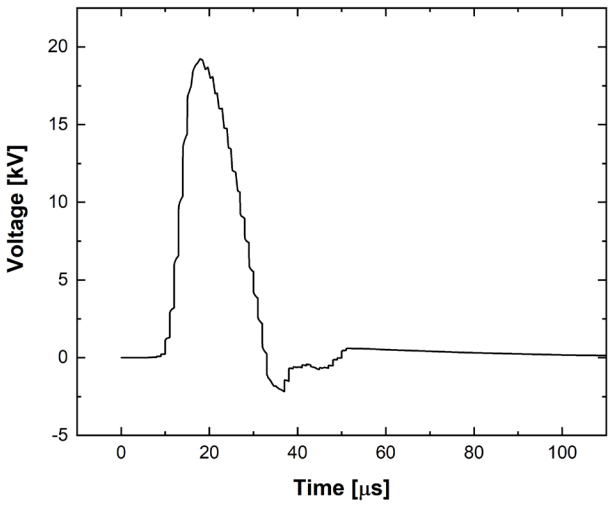

Fig. 8. Voltage waveform applied in the FEM model to inject the test current.

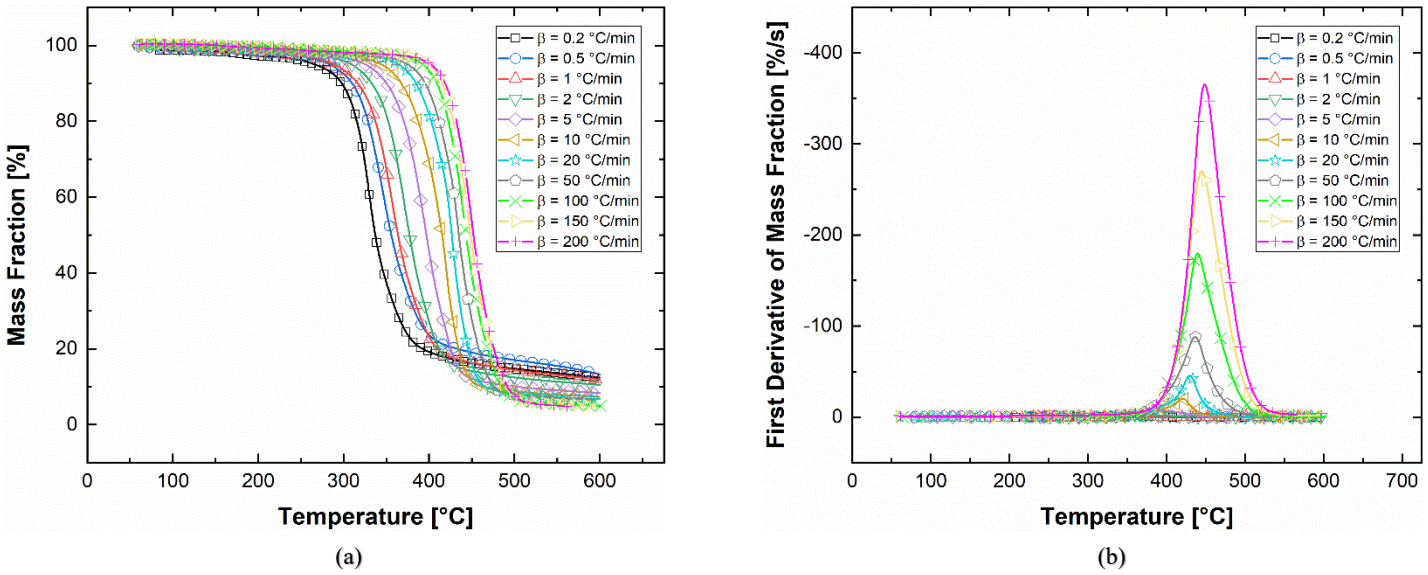

Fig. 9. Thermal degradation of epoxy resin: (a) TGA curves and (b) DTGA curves.

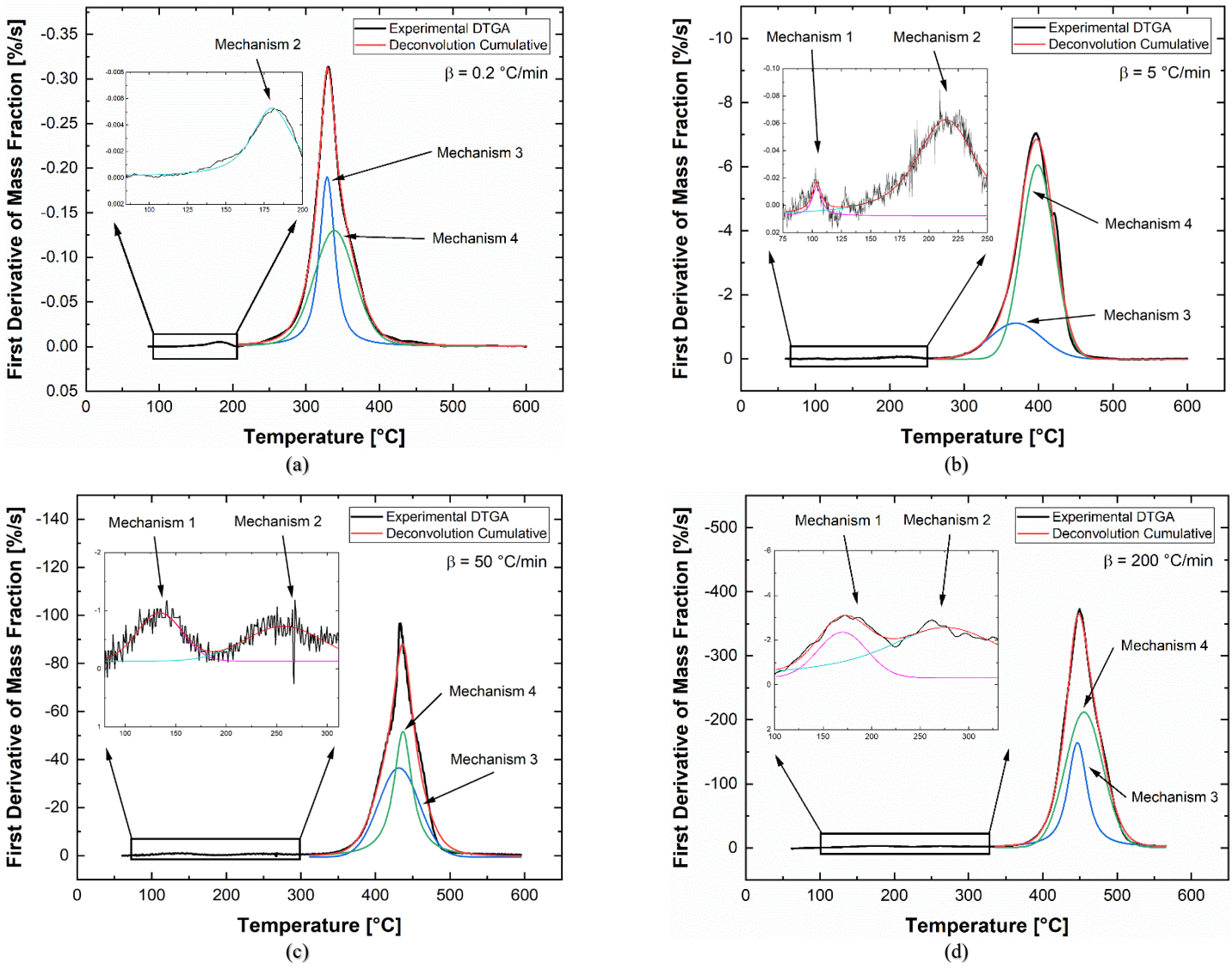

Fig. 10. Deconvoluted reactions DTGA curves at: (a) 0.2 °C/min, (b) 5 °C/min, (c) 50 °C/min, and (d) 200 °C/min.

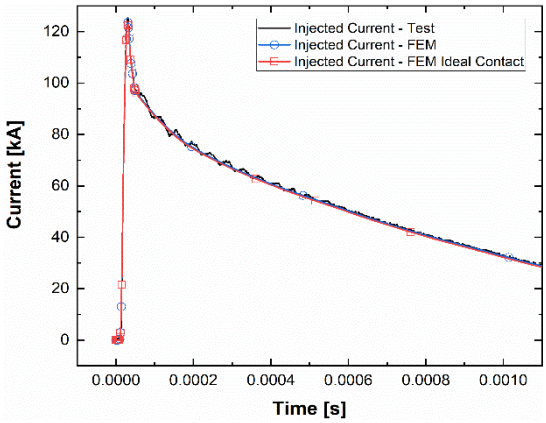

(a)

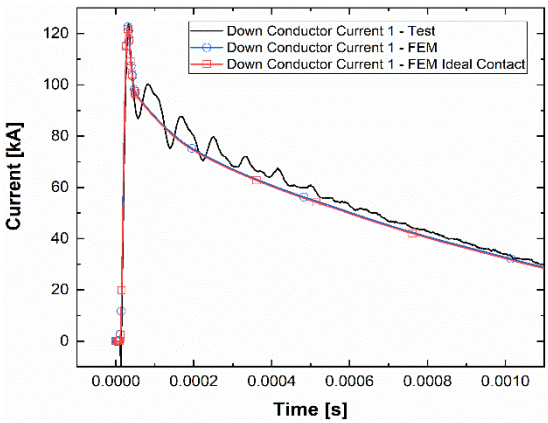

(b)

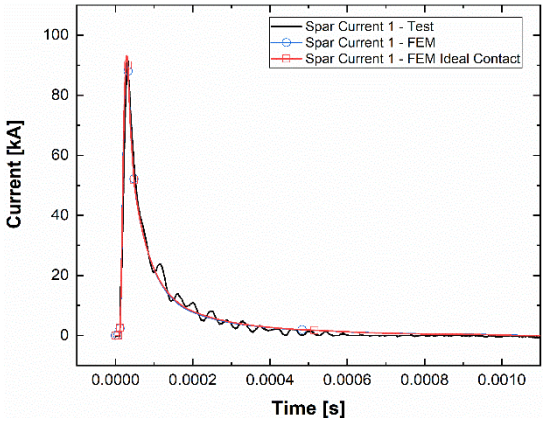

(c)

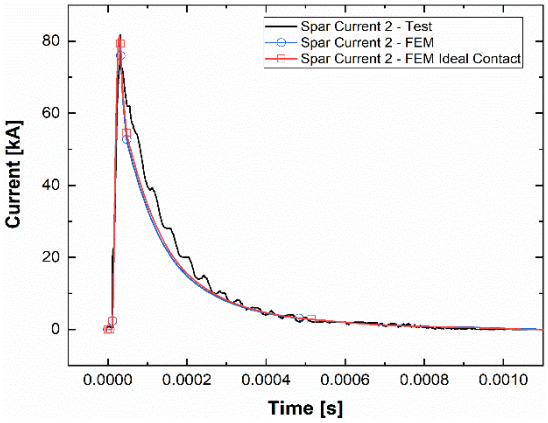

(d)

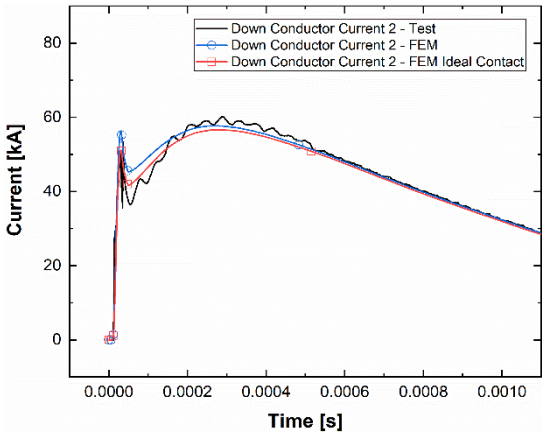

(e)

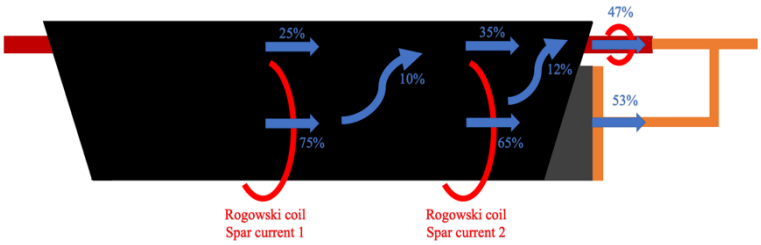

(f)

Fig. 11. Lightning current distribution: (a) injected current, (b) DC current 1, (c) spar current 1, (d) spar current 2, (e) DC current 2, and (f) peak current redistribution along the sample.

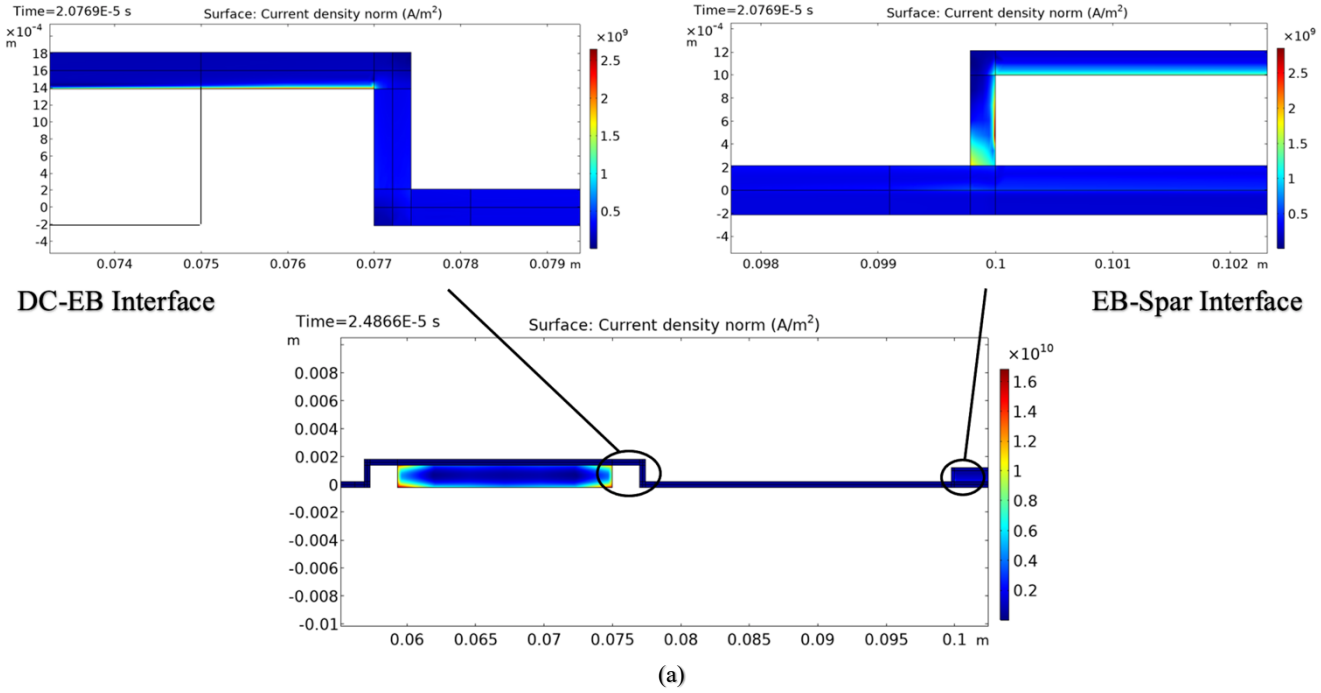

(a)

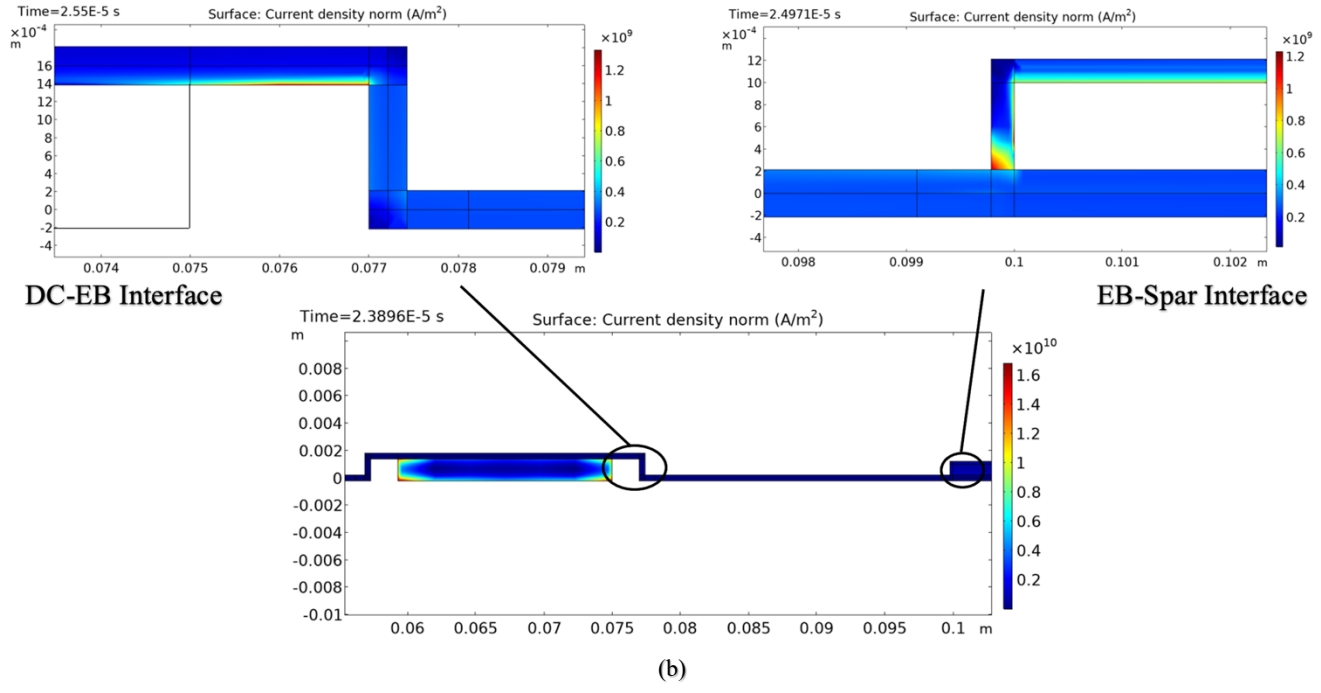

(b)

Fig. 12. High current density areas predicted by the FEM simulations at x = 3.4 m: (a) electrical contact formulation and (b) ideal contact formulation. The interval given in each plot indicates the time of maximum current density.

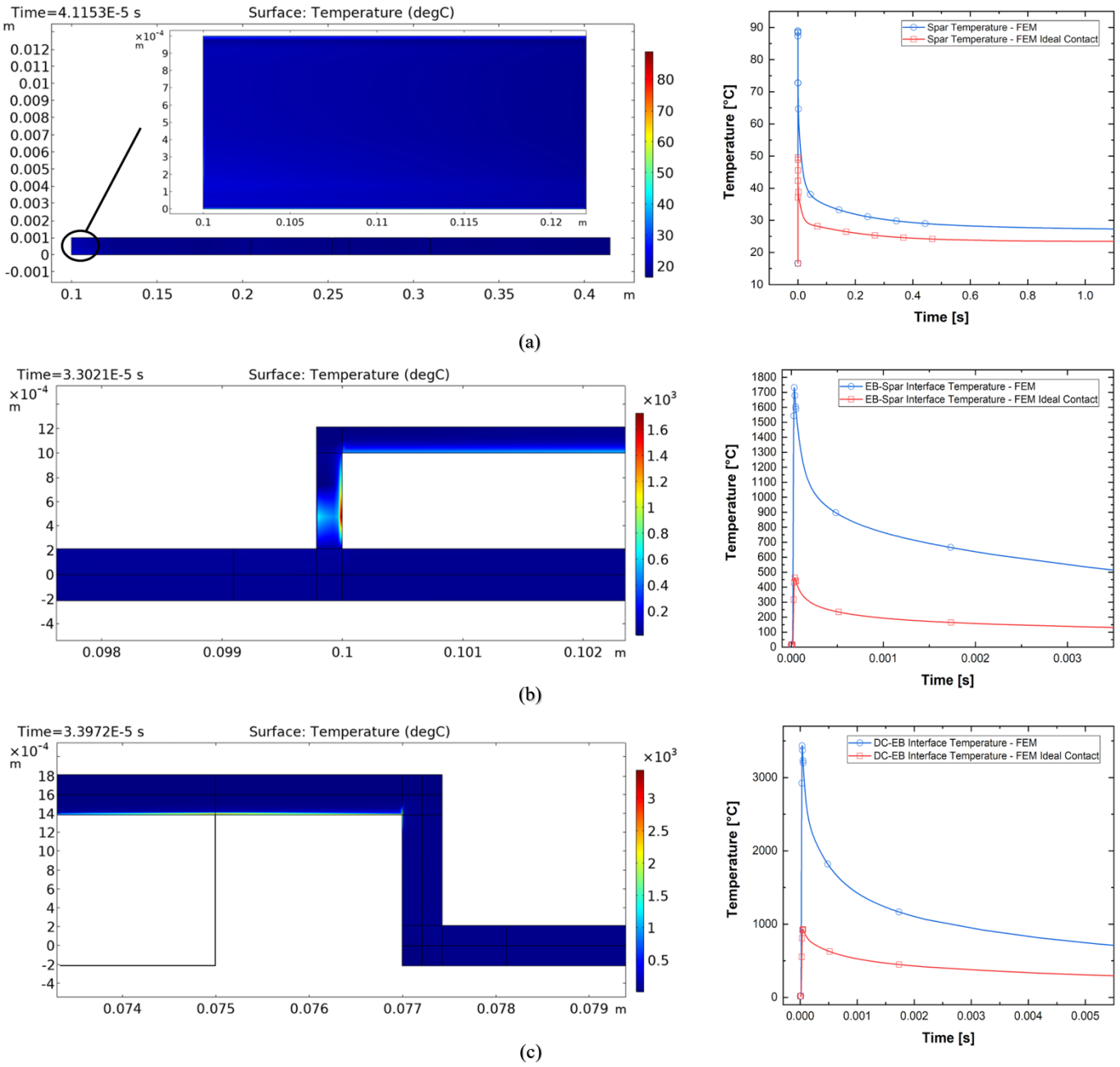

Fig. 13. FEM temperature distribution within the rotor blade sample at x = 3.4 m: (a) spar, (b) EB-Spar interface, and (c) DC-EB interface. The interval given in each plot indicates the time of maximum temperature.

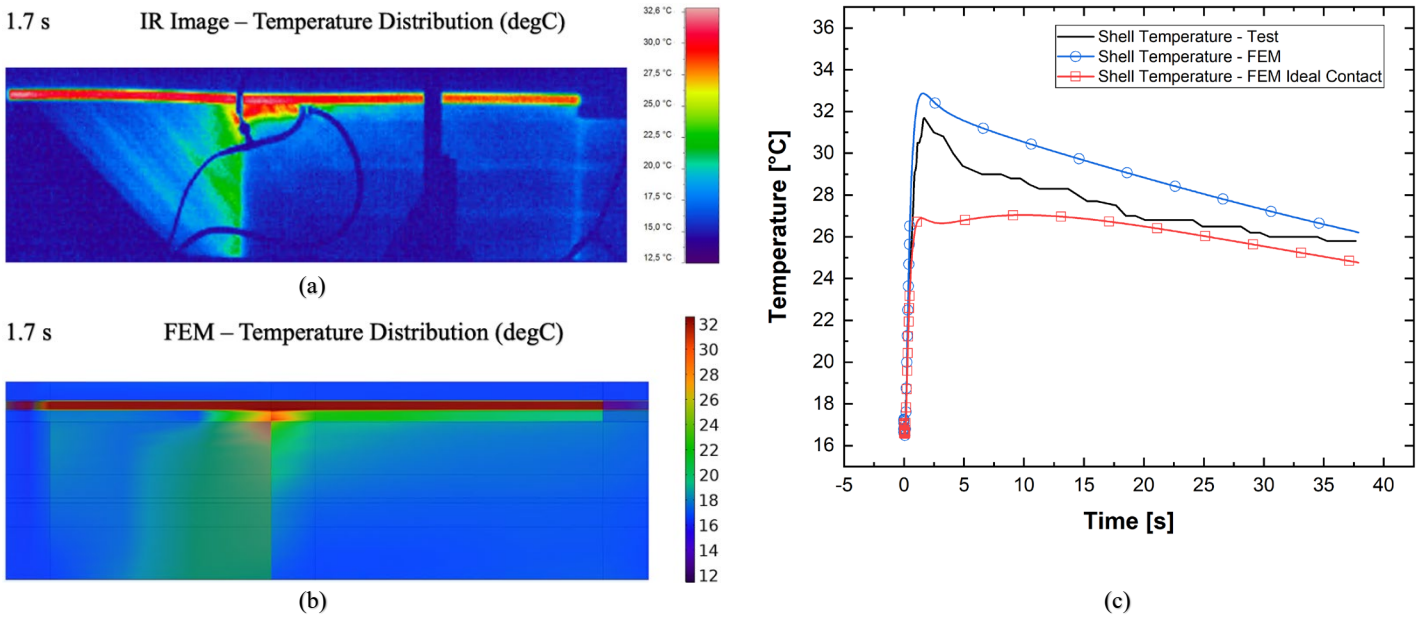

Fig. 14. Temperature distribution on the shell inner layer at the tip end: (a) IR image recorded during the test, (b) FEM temperature distribution, and (c) temperature evolution with time.

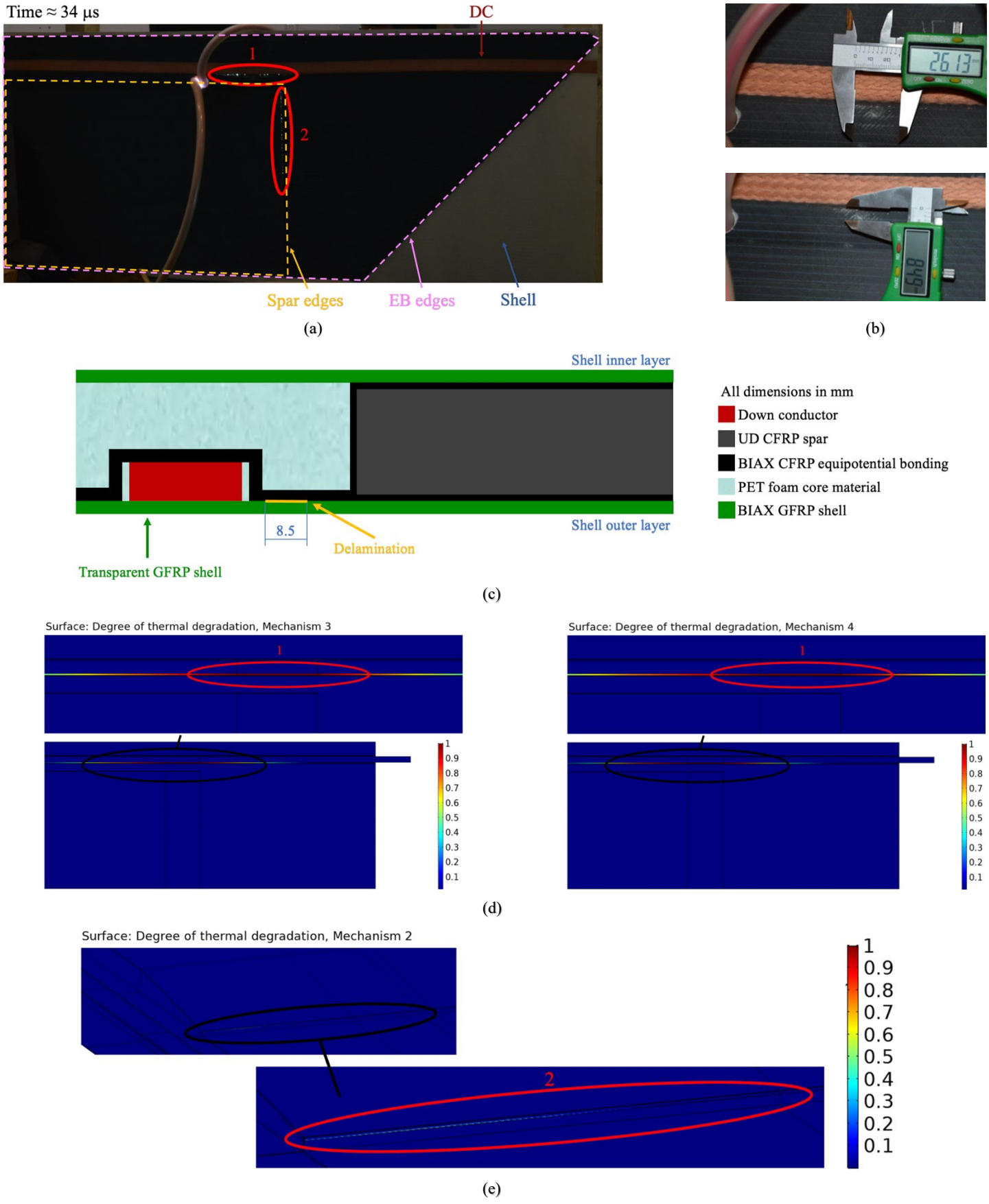

Fig. 15. Comparison between test and numerical observations: (a) sparking locations during the test, (b) delamination, after the test, between the inner surface of the GFRP shell outer layer and the BIAX EB layer, which is visible thanks to the transparency of GFRPs, (c) delamination position in the cross-section view of the sample, (d) FEM polymer thermal degradation at sparking area no. 1, and (e) FEM polymer thermal degradation at sparking area no. 2.